The Astrophysical Journal, 689:563–571, 2008 December 10

A COMPREHENSIVE VIEW OF THE 2006 DECEMBER 13 CME: FROM THE SUN TO INTERPLANETARY SPACE

Y. Liu,[1,2] J. G. Luhmann,[1] R. Müller-Mellin,[3] P. C. Schroeder,[1] L. Wang,[1] R. P. Lin,[1] S. D. Bale,[1] Y. Li,[1] M. H. Acuña,[4] and J.-A. Sauvaud[5]

Received 2008 March 5; accepted 2008 July 17

ABSTRACT

The biggest halo coronal mass ejection (CME) since the Halloween storm in 2003, which occurred on 2006 December 13, is studied in terms of its solar source and heliospheric consequences. The CME was accompanied by an X3.4 flare, EUV dimmings, and coronal waves. It generated significant space weather effects such as an interplanetary shock, radio bursts, major solar energetic particle (SEP) events, and a magnetic cloud (MC) that were detected by a fleet of spacecraft including *STEREO*, *ACE*, *WIND*, and *Ulysses*. Reconstruction of the MC with the Grad-Shafranov (GS) method yields an axis orientation oblique to the flare ribbons. Observations of the SEP intensities and anisotropies show that the particles can be trapped, deflected, and reaccelerated by the large-scale transient structures. The CME-driven shock was observed at both the Earth and *Ulysses* when they were separated by 74° in latitude and 117° in longitude, which is the largest shock extent ever detected. The ejecta seem to have been missed at *Ulysses*. The shock arrival time at *Ulysses* is well predicted by an MHD model that can propagate the 1 AU data outward. The CME/shock is tracked remarkably well from the Sun all the way to *Ulysses* by coronagraph images, type II frequency drift, in situ measurements, and the MHD model. These results reveal a technique that combines MHD propagation of the solar wind and type II emissions to predict the shock arrival time at the Earth, which is a significant advance for space weather forecasting, especially when in situ data become available from the *Solar Orbiter* and *Solar Sentinels*.

Subject headings: shock waves — solar-terrestrial relations — solar wind — Sun: coronal mass ejections (CMEs) — Sun: particle emission — Sun: radio radiation

Online material: color figures, mpeg animation

1. INTRODUCTION

Coronal mass ejections (CMEs) are the most spectacular eruptions in the solar atmosphere and have been recognized as primary drivers of interplanetary disturbances. They are called interplanetary CMEs (ICMEs) when they move into the solar wind. Often associated with CMEs and ICMEs are radio bursts, shock waves, solar energetic particle (SEP) events, and prolonged southward magnetic field components. A southward field component can reconnect with geomagnetic fields and produce storms in the terrestrial environment (e.g., Dungey 1961). Understanding CMEs and characterizing their interplanetary transport are crucial for space weather forecasting but require coordinated multiwavelength observations in combination with in situ measurements.

The 2006 December 13 CME is the largest halo CME since the Halloween storm, which occurred in 2003 October–November (e.g., Gopalswamy et al. 2005; Richardson et al. 2005; Lario et al. 2005), given the observed speeds of the CME and its forward shock, the time duration of the ICME at 1 AU, the SEP intensities, and the angular extent of the shock (see §§ 2 and 3). It is also the largest CME in the era of the *Solar Terrestrial Relations Observatory* (*STEREO*) up to the time of this writing. Differently from the Halloween storm, this event is relatively isolated from other CMEs, so contamination by or mixing with other events is less pronounced; propagation into a solar wind environment near solar minimum would also make theoretical modeling easier. Accompanied by an X3.4 solar flare, the CME evolved into a magnetic cloud (MC) and produced significant space weather effects, including SEP events, an interplanetary shock, and radio bursts detected by various instruments aboard a fleet of spacecraft. Examining the evolution and propagation of this event through the heliosphere would provide benchmark studies for CMEs, associated phenomena, and space weather.

The purpose of this work is to study the solar source and heliospheric consequences of this CME in the frame of the Sun-Earth connection. We combine EUV, coronagraph, radio, in situ particle, plasma, and magnetic field measurements with modeling efforts in an attempt to give a comprehensive view of the event; particular attention is paid to tracking the CME/shock all the way from the Sun far into interplanetary space. We look at EUV and coronagraph images in § 2. Evolution of the CME in the heliosphere and its effects on particle transport are investigated in § 3. In § 4, we combine different data and demonstrate how the CME/shock propagation can be tracked using coordinated observations and magnetohydrodynamic (MHD) modeling. The results are summarized and discussed in § 5.

2. CME AT THE SUN

We look at CME observations from the Large Angle Spectroscopic Coronagraph (LASCO) and coronal observations from the Extreme ultraviolet Imaging Telescope (EIT) aboard the *Solar and Heliospheric Observatory* (*SOHO*). The Sun Earth Connection Coronal and Heliospheric Investigation (SECCHI) of *STEREO* was not turned on at the time of the CME. Figure 1 displays combined images as seen by the EIT and LASCO C2 during the CME. The CME starts with a strong EUV brightening in the southwest

[1] Space Sciences Laboratory, University of California, Berkeley, CA 94720; liuxying@ssl.berkeley.edu.
[2] State Key Laboratory of Space Weather, Chinese Academy of Sciences, Beijing 100080, China.
[3] Institut für Experimentelle und Angewandte Physik, Universität Kiel, D-24098 Kiel, Germany.
[4] NASA Goddard Space Flight Center, Greenbelt, MD 20771.
[5] Centre d'Etude Spatiale des Rayonnements, Centre National de la Recherche Scientifique, F-31028 Toulouse Cedex 4, France.

FIG. 1.— Difference images of the CME and the source region at different times. EIT difference images at 195 Å are shown within the white circles. A transition layer is visible around the CME front, indicating the existence of a shock (*middle and right*). Adapted from the LASCO CME catalog at http://cdaw.gsfc.nasa.gov. [*This figure is available as an mpeg animation in the electronic edition of the Journal.*]

quadrant at 02:30 UT. Around 02:54 UT, it forms a nearly complete halo; the EUV brightening is followed by a dimming that quickly spreads into a diffusive area of the solar disk. The CME moves further out around 03:06 UT and forms a spectacular ring of dense material. The good timing between the dimming and the CME indicates that the reduced EUV brightness results from removal of the coronal plasma due to the lift-off of the CME (e.g., Thompson et al. 1998; Zarro et al. 1999). Depletion of the coronal material by CMEs is possible if the associated magnetic field is opened or stretched into interplanetary space, as proposed by many CME models. Note that a small CME precedes the big event, as can be seen in Figure 1 (*left*). Interactions of successive CMEs are thought to affect SEP production (e.g., Gopalswamy et al. 2004).

Faint diffuse EUV brightenings are also seen and appear to be propagation fronts of the dimming. These brightenings may represent coronal waves propagating away from the active region. They were first discovered by Neupert (1989), but were popularized in EIT observations by Thompson et al. (1998); for that reason they have been referred to as "EIT waves." The low cadence rate of EIT observations (12 minutes for the 195 Å band) does not allow an accurate determination of the speed of the waves to be made. The brightenings moving toward the northeast hemisphere, however, seem to have a constant speed: they travel a distance of $\sim 0.86\,R_\odot$ (where $R_\odot$ is the solar radius) within 24 minutes from 02:24 UT to 02:48 UT and another $0.43\,R_\odot$ within 12 minutes from 02:48 UT to 03:00 UT (see Fig. 1). The speed is estimated to be about 420 km s^{-1}. The CME speed projected on the sky is about 1774 km s^{-1}, as measured along a position angle of 193° (counterclockwise from the north; see CME identification and parameters at the LASCO CME catalog[6]), which is significantly larger than the EIT wave speed. The nature and origin of the coronal waves are not clear, although an unambiguous correlation between EIT waves and CMEs has been established (e.g., Biesecker et al. 2002). An observed metric type II burst starting at 02:27 UT, however, indicates that the present EIT wave is likely a shock wave.

A closer look at the images also reveals a sharp edge all the way around the CME front (see the middle and right panels of Fig. 1), reminiscent of a shock signature. Given the fast expansion of the CME and a density at 1 AU comparable to that of the ambient solar wind (see Fig. 3), the CME density near the Sun must be much larger than the ambient density; the density increase due to shock compression is at most a factor of 4 times that of the background medium. The sheath region (a transition layer between the CME front and the shock) should thus have a brightness weaker than that of the CME, consistent with the coronagraph observations. Therefore, the sharp white-light feature is likely the CME-driven shock. It is very rare to see the shock in white light, especially for halo CMEs (e.g., Vourlidas et al. 2003).

The CME is accompanied by an X3.4 solar flare located in NOAA AR 10930 (S06°W23°). The flare seems to be induced by a strong shear in the magnetic field associated with a filament eruption, leading to two large ribbons that are twisted but largely horizontal around the filament channel (e.g., Zhang et al. 2007; Kosovichev & Sekii 2007). We will compare the orientation of the filament channel with a reconstruction of the associated MC observed in situ (see § 3.1 and Li et al. 2007).

3. INTERPLANETARY CONSEQUENCES

After its abrupt formation in the solar corona, the CME propagated into the interplanetary medium and was observed in situ by *STEREO*, *ACE*, and *Ulysses*. We infer the ICME structure from in situ measurements of plasma and magnetic field parameters combined with a flux rope reconstruction model. Connectivity of the ICME back to the Sun is indicated by energetic particles, which could be channeled, constrained, and reaccelerated by the transient structure.

3.1. *ICME at* 1 AU

STEREO observed the ICME after its exit from the terrestrial magnetosheath. Figure 2 shows *STEREO* in situ measurements across the event made by the Solar Wind Electron Analyzer (SWEA; Sauvaud et al. 2008) and the magnetometer (MAG; Acuña et al. 2008) of the In situ Measurements of Particles And CME Transients investigation (IMPACT; Luhmann et al. 2008). *STEREO A* and *STEREO B* were not well separated, so they observed essentially the same structure. The plasma parameters (e.g., density, velocity, and temperature) are not available from *STEREO* for that time period. Bidirectional streaming electrons (BDEs) seem to be coincident with the strong magnetic fields, indicative of closed field lines within the event; the rotation of the field (see the field elevation angle) indicates an MC. The MC interval is determined from the BDEs but is also consistent with the reduced field variance and the rotation of the field. The magnetic field has a significant negative (southward) component, which caused a major geomagnetic storm with $Dst \sim -190$ nT. Interestingly, there is a current sheet (indicated by the peak of the field elevation angle) within the MC, which might be due to the passage of comet

[6] Available at http://cdaw.gsfc.nasa.gov.

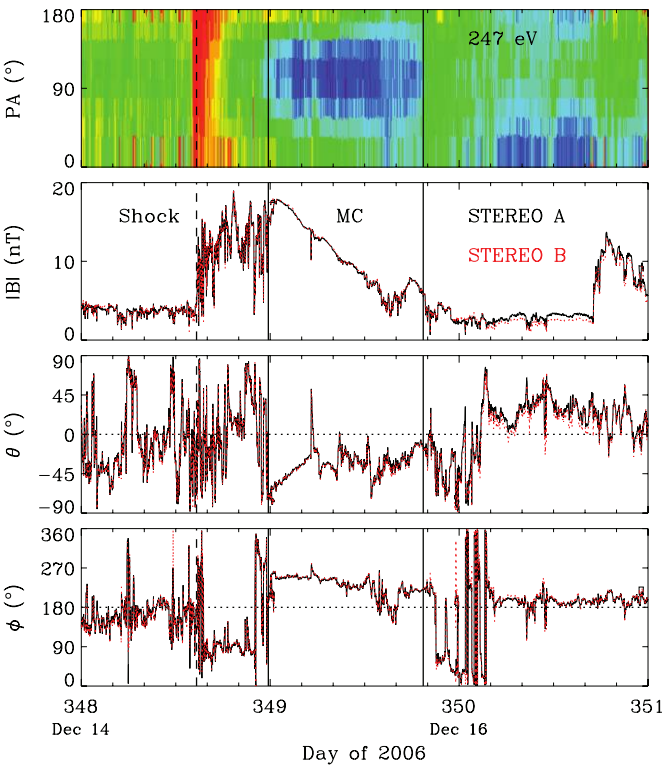

FIG. 2.—Pitch-angle (PA) distribution of 247 eV electrons measured by *STEREO A*, as well as the magnetic field strength and the field elevation and azimuthal angles in RTN coordinates measured by *STEREO A* (*black lines*) and *STEREO B* (*red lines*) across the MC (*bracketed by the two vertical lines*). The vertical dashed line denotes the arrival time of the MC-driven shock. The color shading indicates the values of the electron flux (descending from red to blue).

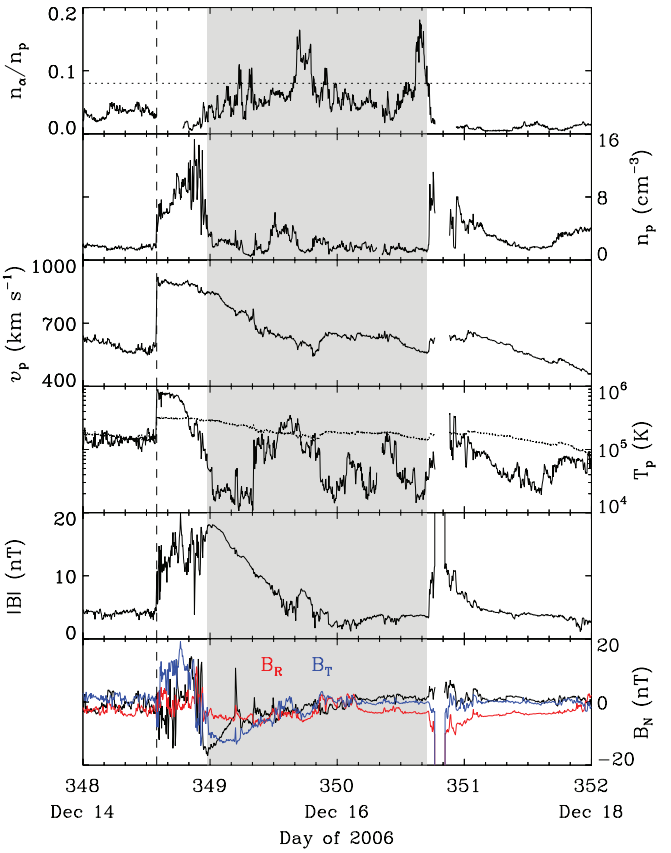

FIG. 3.—Solar wind plasma and magnetic field parameters across the ICME (*shaded region*) observed at *ACE*. From top to bottom, the panels show the alpha/proton density ratio, the proton density, the bulk speed, the proton temperature, the magnetic field strength, and the field components in RTN coordinates. The dotted lines denote the 8% level of the density ratio (*top*) and the expected proton temperature (*fourth from top*), respectively. The arrival time of the shock is marked by the vertical dashed line.

McNaught through the event (C. T. Russell 2007, private communication). The magnetic field trailing behind the MC has a roughly constant direction, presumably stretched by the MC because of its large speed. A preceding shock, as can be seen from simultaneous increases in the electron flux and magnetic field strength, passed the spacecraft at 14:38 UT on December 14. The transit time is about 36 hr from the Sun to the Earth (assuming a launch time at 02:30 UT on December 13), which suggests an average speed of $\sim$1160 km s^{-1}. This speed is significantly smaller than the white-light speed close to the Sun (1774 km s^{-1}) but larger than the shock speed at 1 AU (1030 km s^{-1}; see below), so the shock must be decelerated as the high-speed flow overtakes the preceding solar wind. The propagation of the shock, as well as the deceleration, is calculated in § 4.

Complementary plasma parameters from *ACE* are displayed in Figure 3; the magnetic field is almost the same as that measured at *STEREO*. The ICME interval is identified by combining the enhanced helium/proton density ratio and depressed proton temperature (as compared with the normal temperature expected from the observed speed); the boundaries also agree with the discontinuities in the density, bulk speed, and magnetic field. The resulting radial width (average speed times the duration) is about 0.67 AU; the MC indicated by *STEREO* BDEs is about the first half of the time interval. The preceding shock is also apparent from the plasma parameters. The shock speed is about 1030 km s^{-1} as calculated from the conservation of mass across the shock; i.e., $v_s = (n_2v_2 - n_1v_1)/(n_2 - n_1)$, where $n_1 = 1.8$ cm^{-3}, $n_2 = 6.0$ cm^{-3}, $v_1 = 573$ km s^{-1}, and $v_2 = 896$ km s^{-1} are the average densities and speeds upstream (1) and downstream (2) of the shock, respectively. As shown above, the shock has to be decelerated when propagating from the Sun to the Earth. A least-squares fit of the plasma and magnetic field data across the shock to the Rankine-Hugoniot relations (Viñas & Scudder 1986) gives a shock normal with an elevation angle of $\theta \simeq -12.7^\circ$ and an azimuthal angle of $\phi \simeq 308^\circ$ in RTN coordinates (with $\boldsymbol{R}$ pointing from the Sun to the spacecraft, $\boldsymbol{T}$ parallel to the solar equatorial plane and along the planet motion direction, and $\boldsymbol{N}$ completing the right-handed system). The shock normal makes an angle of about 56° with the upstream magnetic field, so the shock may be quasi-perpendicular. Liu et al. (2006a) find that the sheath regions between fast ICMEs and their preceding shocks are analogous to planetary magnetosheaths and are often characterized by plasma depletion layers and mirror-mode waves. The proton density in the sheath of the current event first increases and then decreases quickly close to the MC, very similarly to the case shown in their Figure 3. Magnetic fluctuations in the sheath appear to be consistent with mirror-mode waves, but note that large depressions are due to current sheet crossings; a quasi-perpendicular shock would heat the plasma preferentially in the direction perpendicular to the field, so the plasma downstream of the shock may be unstable to the mirror-mode instability (e.g., Liu et al. 2007). There seems to be another ICME on December 17, as can be seen from the low proton temperature and declining speed. Interactions between the two events are likely to be present.

We reconstruct the MC structure using the Grad-Shafranov (GS) technique, which includes the thermal pressure and can give a cross section without prescribing the geometry (e.g., Hau & Sonnerup 1999; Hu & Sonnerup 2002). This method relies on the feature

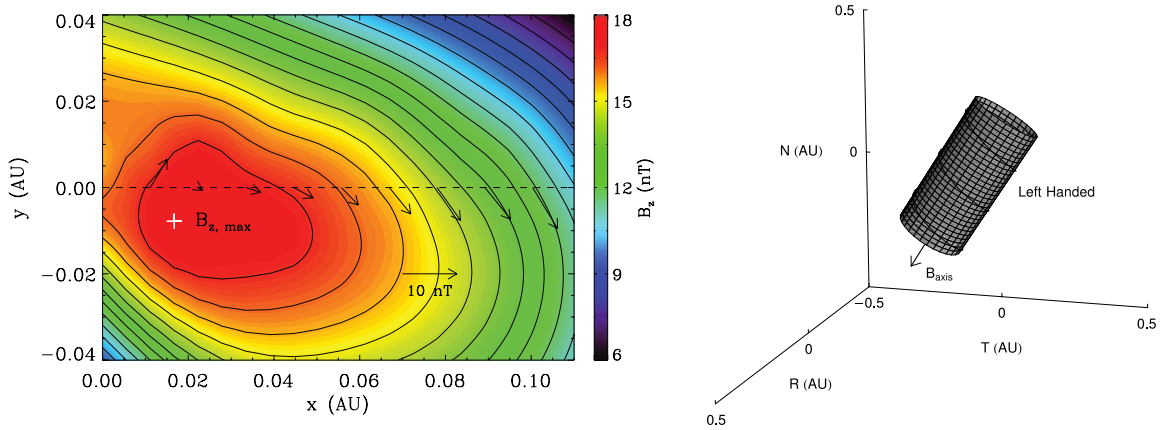

FIG. 4.—*Left*: Reconstructed cross section of the MC. Black contours show the distribution of the vector potential, and the color shading indicates the value of the axial field. The dashed line marks the trajectory of the spacecraft. The arrows denote the direction and magnitude of the observed magnetic fields projected onto the cross section. The location of the maximum axial field is indicated by the plus sign. *Right*: Idealized schematic diagram of the MC approximated as a cylindrical flux rope in RTN coordinates, with the arrow and the helical line indicating the field orientation. [*See the electronic edition of the Journal for a color version of the right panel of this figure.*]

that the thermal pressure and the axial magnetic field depend on the vector magnetic potential only (Schindler et al. 1973; Sturrock 1994, p. 209), which has been validated by observations from *STEREO* and *ACE*/*WIND* when these spacecraft are well separated (Liu et al. 2008). We apply the method to the plasma and magnetic field data between 22:48 UT on December 14 (the MC leading edge) and 04:34 UT on December 15 (right before the current sheet within the MC) when the magnetic field has the clearest rotation. All the data used in the reconstruction are from the MC interior. The reconstruction results are illustrated in Figure 4. The recovered cross section (in a flux rope frame with $\boldsymbol{x}$ along the spacecraft trajectory and z in the direction of the axial field) shows nested helical field lines, suggestive of a flux rope structure. The spacecraft (*ACE* and *STEREO*) seem to cross the MC close to the axis, with an impact parameter of 0.01 AU; the maximum axial field is also very close to the leading edge ($x = 0$). The transverse fields along the spacecraft path indicate a left-handed chirality. The reconstruction gives an axis elevation angle of $\theta \simeq -57^\circ$ and an azimuthal angle of $\theta \simeq 261^\circ$ in RTN coordinates, as shown in Figure 4 (*right*). Since the axial field points southward and the field configuration is left-handed, a spacecraft would see a field that is first most negative and then becomes less negative as the MC passes the spacecraft along the radial direction. These results are consistent with observations (see Figs. 2 and 3). We also apply the method to a larger interval inside the MC (with the current sheet excluded) and obtain a similar cross section and axis orientation. Note that the axis orientation is oblique to the filament channel; similar results are obtained for other cases (e.g., Wang et al. 2006). The MC axis orientation depends on which part of the CME is observed in situ; another factor that could affect the axis orientation is that the CME may rotate during its propagation in the heliosphere.

3.2. *SEP Events*

Major SEP events are observed at 1 AU during the ICME passage. The ICME structure, as well as its effects on energetic particle transport, can also be inferred from particle measurements. Figure 5 shows the particle intensities measured by the Electron, Proton, and Alpha Monitor (EPAM) of *ACE* and the Solar Electron and Proton Telescope (SEPT) of *STEREO A*. Four particle enhancements are evident. The timing with the flares and shocks indicates that the first particle enhancement is associated with the injection from the X3.4 flare (02:38 UT on December 13), the second one with the ICME forward shock (14:38 UT on December 14), the third one with an X1.5 flare (22:14 UT on December 14) that occurred in the same active region (NOAA AR 10930; S06°W46°), and the fourth one with the shock downstream of the ICME (17:23 UT on December 16; see Figs. 2 and 3). The X3.4 flare produced an intense electron flux that declines during a long time period; velocity dispersion is not clear in the electrons but is present in the protons. Note that the CME-driven shock should be producing energetic particles throughout the interplanetary transit.

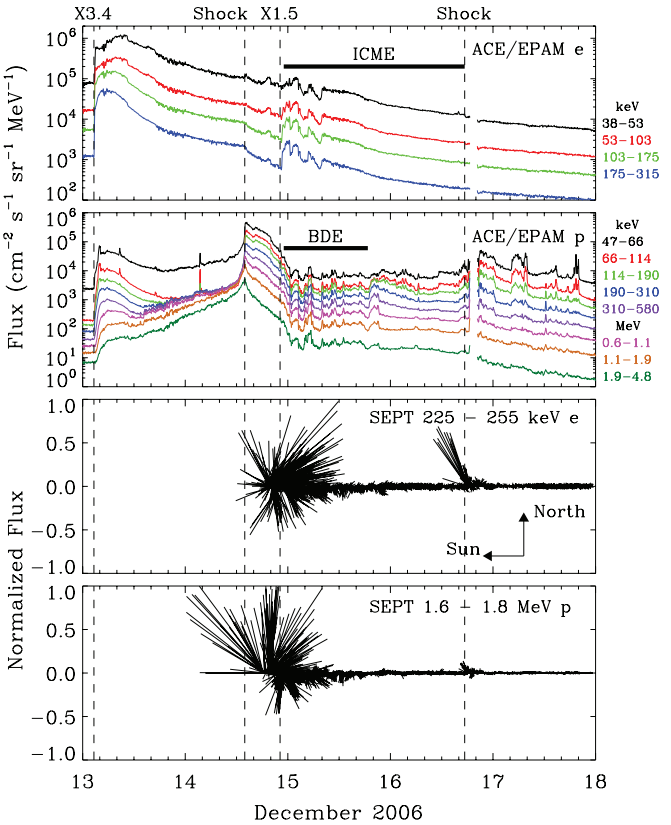

FIG. 5.—Intensities of electrons (*top*) and protons (*second from top*) at different energy channels measured by the *ACE* EPAM, and anisotropies of electrons (*third from top*) and protons (*bottom*) observed by the *STEREO A* SEPT. The times of the flares and shocks are marked by the vertical dashed lines. The ICME and BDE intervals are indicated by the horizontal bars. The solid lines in the two bottom panels denote the normalized intensity differences along the directions defined by the arrows (*third from top*).

It continues to accelerate protons to ~MeV energies at 1 AU but appears to have a small effect on the electrons, probably because the electron enhancement at the shock is masked by the large preshock intensities. There is an apparent exclusion of the protons from the ICME interior (see Fig. 5, *second from top*), which are presumably screened off by the strong fields within the ICME; the proton signature also seems to be consistent with the BDE interval. Interestingly, there is an intensity enhancement of the electrons within the ICME due to the X1.5 flare; it is likely that the electrons stream along the field line from the active region and are trapped inside the ICME (e.g., Kahler & Reames 1991; Larson et al. 1997), so the ICME may still be magnetically connected to the Sun. These features are very similar to observations during the Halloween storm (e.g., Malandraki et al. 2005; McKibben et al. 2005).

The two bottom panels in Figure 5 show anisotropy information of the particles, provided by the *STEREO A* SEPT. SEPT has two separate telescopes, one looking in the ecliptic plane along the nominal Parker spiral field toward and away from the Sun and the other looking vertical to the plane toward the south and north, respectively (Müller-Mellin et al. 2008). The lines in the two panels represent the intensity differences between the two directions for each telescope (i.e., differences between south and north and between the two opposite directions along the Parker field); the intensity difference is normalized by 4000 $cm^{-2}\ s^{-1}\ sr^{-1}\ MeV^{-1}$ for the electrons and by 1000 $cm^{-2}\ s^{-1}\ sr^{-1}\ MeV^{-1}$ for the protons. The data before 18:10 UT on December 14 are discarded, because the SEPT doors had been closed since the launch of *STEREO* and were opened one by one from 17:32 UT to 18:10 UT on December 14. The anisotropy information of the particles is thus not available before 18:10 UT on December 14. The X1.5 flare produced electrons and protons moving largely antisunward at 1 AU, but some antisunward particles may have been mirrored back by the enhanced magnetic fields in the ICME/sheath and then propagated in the sunward direction. A beam of particles that were accelerated at the second shock, which may also have been deflected by the first ICME, moves sunward and northward.

Further information about the electron behavior across the ICME is provided by SWEA and the suprathermal electron instrument (STE; Lin et al. 2008) on board *STEREO*, as shown in Figure 6. The electron energies range from ~1 eV to 100 keV. The pitch-angle distribution of the 247 eV electrons displayed in Figure 2 is measured by SWEA in the spacecraft frame; BDE signatures are discernible from ~50 eV to ~1.7 keV for this event. There seems to be a flux decrease associated with the BDE interval; the high-energy electrons from STE recover before the trailing edge of the BDE interval, earlier than the low-energy electrons. The electron intensity profiles are quantitatively different from what is shown in Figure 5, which may be due to the different directions in which the detectors were looking and different connectivities of the spacecraft via the magnetic field line to the Sun.

The above results suggest that the particle transport is largely governed by the large-scale transient structures. The particles can be deflected and constrained by ICMEs and reaccelerated by their associated shocks, so modeling of the particle transport is complicated by the presence of these structures. The energetic particles, however, could be used to trace the ICME structure, which can then be compared with plasma and magnetic field measurements. More information on ion intensities, spectra, and composition regarding the events can be found in Mewaldt et al. (2008) and Mulligan et al. (2008).

3.3. *ICME at Ulysses and Beyond*

Ulysses was at a distance of 2.73 AU, with a latitude of -74.9° and a longitude of 123.3° in the heliographic inertial system, when

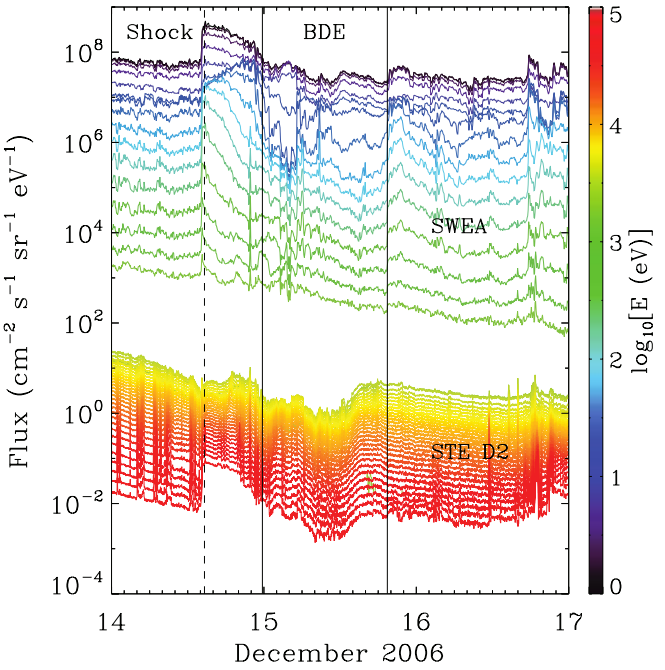

FIG. 6.— Electron intensities across the BDE interval (between the solid lines) measured by SWEA and STE D2 (one of the detectors looking away from the Sun) aboard *STEREO B*. The color scale shows the electron energies. The shock arrival time is indicated by the dashed line.

it observed a large shock at 17:02 UT on December 17. *Ulysses* was about 117° east and 74° south of the Earth. The large spacecraft separation provides a great opportunity to measure the spatial extent of the CME-driven shock. Figure 7 displays the *Ulysses* data for a 5 day interval. The shock is apparent from the sharp increases in the plasma and magnetic field parameters. During this time period, there are no clear ICME signatures such as enhanced helium abundance, depressed proton temperature, or smooth strong magnetic fields compared with the ambient solar wind upstream of the shock. It is likely that the ICME was missed at *Ulysses*, whereas the shock was observed. The shock has a speed of about 870 km s^{-1}, which is smaller than the 1 AU speed (1030 km s^{-1}), but not significantly so. Given a speed difference of more than 740 km s^{-1} between that at the Sun and that at 1 AU, the primary deceleration of the shock must occur within 1 AU, and further out the shock moves with a roughly constant speed. Propagation of the shock from the Sun to *Ulysses* is quantified in § 4 by combining the coronagraph, radio, and in situ data with an MHD model. The shock normal has an elevation angle of $\theta \simeq -38.3^\circ$ and an azimuthal angle of $\phi \simeq 77.5^\circ$ (in RTN coordinates), resulting from the Rankine-Hugoniot calculations (Viñas & Scudder 1986). The angle between the shock normal and the upstream magnetic field is about 68°, so the shock is also quasi-perpendicular at *Ulysses*.

To show that *Ulysses* observed the same shock as *ACE*/*STEREO*, we propagate the solar wind data outward from 1 AU using an MHD model (Wang et al. 2000). The model has had success in connecting solar wind observations at different spacecraft (e.g., Wang et al. 2001; Richardson et al. 2002, 2005, 2006; Liu et al. 2006b). The model assumes spherical symmetry (one-dimensional), since we have solar wind measurements at only a single point. We use the solar wind parameters observed at 1 AU (an interval of 50 days around the ICME) as input to the model and propagate the solar wind outward. Figure 8 shows the observed speeds at 1 AU and *Ulysses* and the model-predicted speeds at certain distances. Small streams smooth out due to stream interactions, as can be seen from the traces, but the large stream associated with

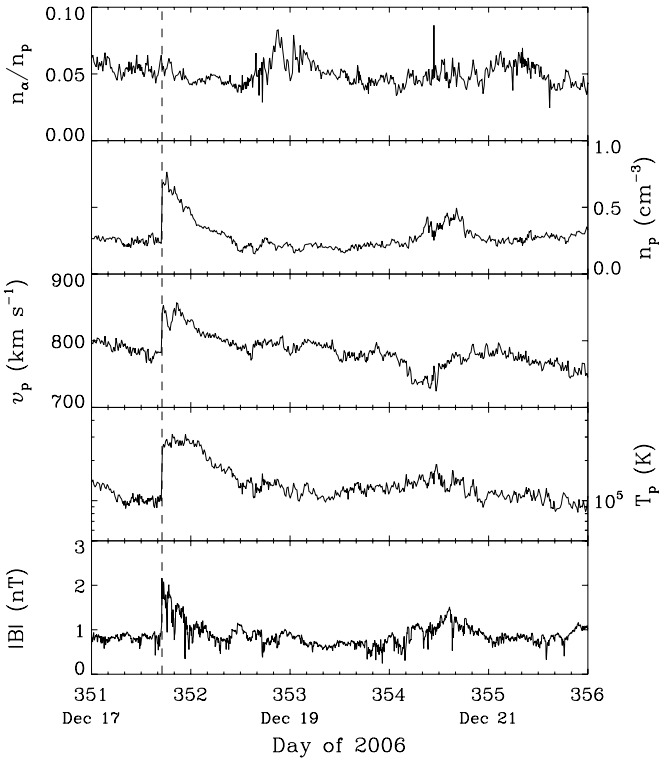

FIG. 7.—Similar format to Fig. 3, but for the measurements at *Ulysses*.

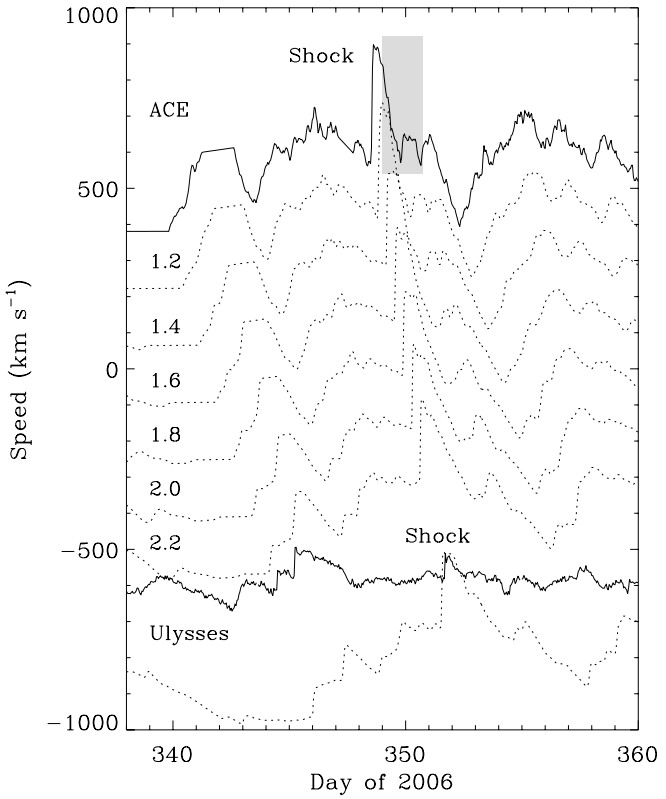

FIG. 8.—Evolution of solar wind speeds from *ACE* to *Ulysses* via the MHD model. The shaded region represents the ICME interval at *ACE*. The upper and lower solid lines show the solar wind speeds observed at *ACE* and *Ulysses*, respectively. The dotted lines denote the predicted speeds at the distances (in units of AU) marked by the numbers; each curve is decreased by 160 km s^{-1} with respect to the previous one so that the individual profiles are discernible. The speed profiles at *Ulysses* (both observed and predicted) are shifted downward by 1360 km s^{-1} from the 1 AU speeds.

the shock persists out to *Ulysses*. The predicted arrival time of the shock at *Ulysses* is only about 3.6 hr earlier than that observed. The time difference is negligible compared with the propagation time of ~75.1 hr from *ACE* to *Ulysses*. The ambient solar wind predicted by the model is slower than that observed at *Ulysses*, which is reasonable, since *Ulysses* is at the south pole (74° south of *ACE*). Given the good stream alignment, we think that *Ulysses* and the near-Earth spacecraft observed the same shock. *Ulysses* may be observing the shock flank if the nose of the ICME is close to the ecliptic plane. The successful model-data comparison also indicates that the global shock surface is nearly spherical and the shock speed variation from the shock nose to flank is small. It is surprising that even at the south pole the shock is still observed; observations of the same shock by spacecraft configured as above (i.e., one close to the solar equatorial plane and the other at the pole) are rare. Note that the longitudinal size of the shock is also large, with a lower limit of 117° (the longitudinal separation between the Earth and *Ulysses*).

The large size of the shock indicates that the global configuration of the solar wind can be altered as the CME sweeps through the heliosphere. We also propagate the solar wind to large distances using the MHD model. The peak solar wind speeds quickly decrease as the high-speed flow interacts with the ambient medium. They are reduced to 630 km s^{-1} at 10 AU and to 490 km s^{-1} (close to the ambient level) by 50 AU. Therefore, the high-speed streams would not produce significant effects at large distances.

4. CME/SHOCK PROPAGATION

Of particular interest for space weather forecasting is the CME/shock propagation in the inner heliosphere. In the absence of observations of plasma features, propagation of shocks within 1 AU can be characterized by type II radio emissions (e.g., Reiner et al. 2007). Type II radio bursts, typically drifting downward in frequency, are remote signatures of a shock moving through the heliosphere and driving plasma radiation near the plasma frequency and/or its second harmonic (e.g., Nelson & Melrose 1985; Cane et al. 1987). The frequency drift results from the decrease of the plasma density as the shock propagates away from the Sun. The plasma frequency, $f_p = 8.97\sqrt{n}$, where f_p is in units of kHz and n is in units of cm^{-3}, can be converted to a heliocentric distance r (in units of AU) by assuming a density model in which $n = n_0/r^2$:

$$r = \frac{8.97\sqrt{n_0}}{f_p}, \quad (1)$$

where n_0 is the plasma density at 1 AU. The height-time profile of the shock propagation can then be obtained from the frequency drift.

Figure 9 displays the dynamic spectrum, as well as the soft X-ray flux, associated with the CME. An intense type III radio burst occurred at about 02:25 UT on December 13 (Day 347), almost coincident with the peak of the X-ray flux. Type III bursts are produced by near-relativistic electrons escaping from the flaring site (e.g., Lin et al. 1973), so they drift very rapidly in frequency and appear as almost vertical features in the dynamic spectrum. Such an intense type III burst often indicates a major CME (Reiner et al. 2001). Note that many short-lived type III–like bursts are also seen, starting at 17:00 UT on December 13; they are known as type III storms and are presumably associated with a series of small electron beams being injected from the Sun. Diffuse type II emissions occur at the fundamental and harmonic plasma frequencies and appear as slowly drifting features. They start after the

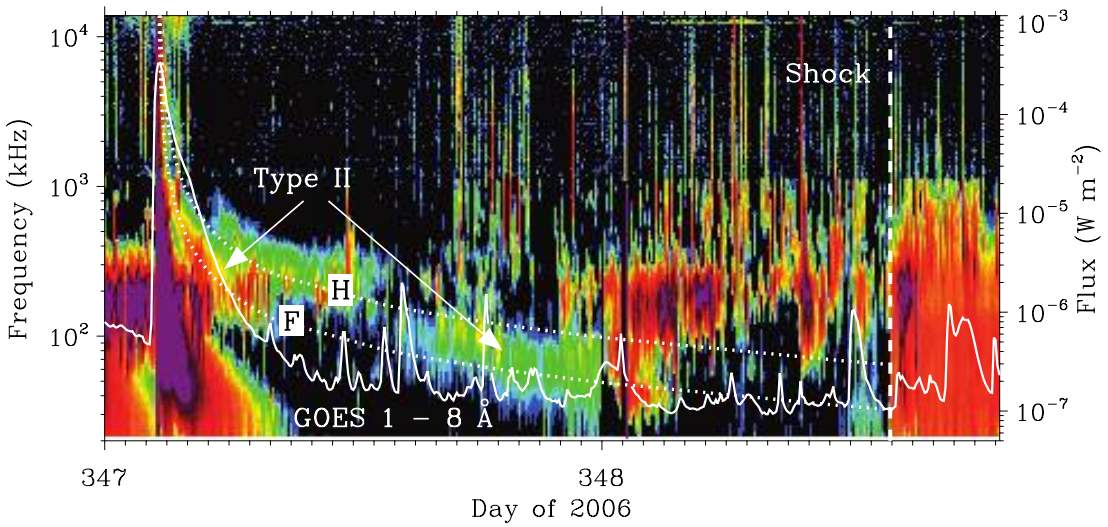

FIG. 9.— Dynamic spectrum (*colors*) from *WIND* WAVES and X-ray flux (*solid line*) from *GOES 12*. The dashed vertical line indicates the arrival time of the preceding shock at 1 AU, and the dotted lines represent the best fits of the frequency drift of the fundamental (F) and harmonic (H) type II bursts.

type III burst and seem to be disrupted during the small flares around 13:00 UT on December 13 (see the X-ray flux). It is not clear whether the type II emissions after 16:00 UT on December 13 are at the fundamental or harmonic of the plasma frequency; the broad band may result from merging of the two branches. Apparently it is difficult to measure the frequency drift from individual frequencies associated with the type II bursts. An overall fit combined with in situ measurements at 1 AU would give a more accurate estimate for the height-time profile.

We employ a kinematic model to characterize the CME/shock propagation, similar to the approach of Gopalswamy et al. (2001) and Reiner et al. (2007). The shock is assumed to start with an initial speed v_0 and a constant deceleration a lasting for a time period t_1, and thereafter it moves with a constant speed v_s. The shock speed v_s and transit time t_T are known from 1 AU measurements, which leaves only two free parameters in the model (a and t_1). At a time t, the distance of the shock can be expressed as

$$r = \begin{cases} d + v_s(t - t_T) + a\left(\frac{1}{2}t^2 + \frac{1}{2}t_1^2 - t_1 t\right), & t < t_1, \\ d + v_s(t - t_T), & t \geq t_1, \end{cases} \quad (2)$$

where $d = 1$ AU and $v_0 = v_s - at_1$. The trace of the fundamental branch of the type II bursts is singled out using an interactive program and is shown in Figure 10; the selected frequencies are converted to heliocentric distances using equation (1). We adjust the density scale factor n_0 so as to obtain a best fit of the frequency drift; a value of $n_0 \simeq 13$ cm^{-3} gives a height-time profile that simultaneously matches the radio data and the shock parameters at 1 AU. The density model describes the average radial variation of the ambient density, so the scale factor is not necessarily the observed plasma density upstream of the shock at 1 AU. Two curves corresponding to the emissions at the fundamental and harmonic plasma frequencies are obtained from the best fit, as is shown in Figure 9. The fit is forced to be consistent with the overall trend of the frequency-drifting bands; discrepancies are seen at some times, due to irregularities of the type II emissions. Note that the best fit yields the radial kinematic parameters of the CME/shock propagation with projection effects minimized. The radial velocity of the shock near the Sun given by the best fit is $v_0 \simeq 2212$ km s^{-1}, which is larger than the measured CME speed projected onto the sky (1774 km s^{-1}). The deceleration is about -34.7 m s^{-2}, lasting for ~9.5 hr, which corresponds to a distance of about 0.36 AU. Thereafter the shock moves with a constant speed of 1030 km s^{-1} as measured at 1 AU.

In order to show how well the CME/shock is tracked by the fit, we extend the curve to the distance of *Ulysses* and plot in Figure 10 the CME locations measured by LASCO (see the LASCO CME catalog[7]), the MHD model output of the shock arrival times at every 0.2 AU between 1 and 2.6 AU, and the shock arrival time at *Ulysses*. The fit agrees with the LASCO data, the MHD model output at different distances, and finally the *Ulysses* measurement. Note that we only use the type II frequency drift and the 1 AU shock parameters to obtain the height-time profile. Even at large distances, the shock is still tracked remarkably well by the fit.

[7] Available at http://cdaw.gsfc.nasa.gov.

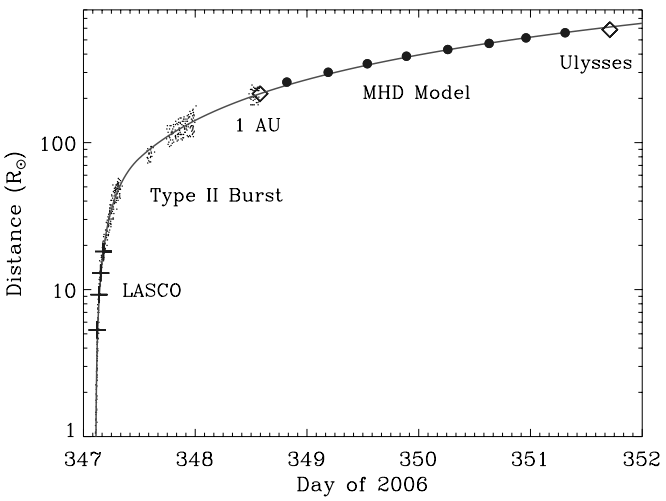

FIG. 10.— Height-time profile (*solid line*) of shock propagation determined from the frequency drift of the type II bands (*dots*) and shock parameters measured at 1 AU (where $R_\odot$ is the solar radius). Plus signs denote the LASCO data. Diamonds indicate the shock arrival times at 1 AU and *Ulysses*. Between 1 AU and *Ulysses* are the shock arrival times (*filled circles*) at 1.2, 1.4, 1.6, 1.8, 2.0, 2.2, 2.4, and 2.6 AU predicted by the MHD model. [*See the electronic edition of the Journal for a color version of this figure.*]

The agreement verifies the kinematic model for the CME/shock propagation; a value of 2212 km s^{-1} should be a good estimate of the CME radial velocity near the Sun. The separation between the shock and the CME should be very small near the Sun but is not negligible at 1 AU (see Figs. 1 and 3).

These results present an important technique for space weather forecasting, especially when in situ measurements closer to the Sun are available (say, from the *Solar Orbiter* and *Solar Sentinels*). In situ data closer to the Sun can be propagated to 1 AU by an MHD model; further constraints on the height-time profile are provided by the frequency drift of type II emissions. The advantage of this method is that the shock can be tracked continuously from the Sun all the way to 1 AU; the arrival time of CME-driven shocks at the Earth can be predicted with an accuracy of less than a few hours, days before they reach the Earth. Implementation of the method, specifically combining MHD propagation of the solar wind with type II frequency drift, is expected to be a routine possibility in the future when in situ data are available from the *Solar Orbiter* and *Solar Sentinels*.

5. SUMMARY AND DISCUSSION

We have investigated the evolution and propagation of the 2006 December 13 CME, combining remote sensing and in situ measurements with modeling efforts. A comprehensive view of the CME is made possible by coordinated EUV, coronagraph, radio, particle, and in situ plasma and magnetic field observations provided by a fleet of spacecraft including *SOHO*, *STEREO*, *ACE*, *WIND*, and *Ulysses*.

The CME is accompanied by an X3.4 solar flare, EUV dimmings, and EIT waves. It had a speed of about 1774 km s^{-1} near the Sun and produced SEP events, radio bursts, an interplanetary shock, and a large ICME embedded with an MC that gave rise to a major geomagnetic storm. The speed of the CME-driven shock is about 1030 km s^{-1} at 1 AU, suggestive of a significant deceleration between the Sun and 1 AU. Reconstruction of the MC with the GS method indicates a flux rope structure with an axis orientation oblique to the flare ribbons. We observe major SEP events at 1 AU, whose intensities and anisotropies are used to investigate the ICME structure. The ICME is still magnetically connected to the Sun, as indicated by the electron enhancement due to the X1.5 flare within the ICME. Particle deflection and exclusion by the ICME suggest that the energetic particle transport is largely dominated by the transient structures.

The CME-driven shock is also observed at *Ulysses*, while the ICME seems to have been missed. *Ulysses* was 74° south and 117° east of the Earth, which indicates a surprisingly large angular extent of the shock. The shock speed is about 870 km s^{-1}, comparable to its 1 AU counterpart. An MHD model using the 1 AU data as input successfully predicts the shock arrival time at *Ulysses* with a deviation of only 3.6 hr, which is substantially smaller than the propagation time of 75.1 hr from *ACE* to *Ulysses*. The model results also show that the peak solar wind speeds quickly decrease at large distances. Consequently, the CME/shock would not cause large effects in the outer heliosphere.

To the best of our knowledge, this may be the largest CME-driven shock ever detected in the space era. *Ulysses*, launched in 1991, is the only spacecraft that can explore the solar wind conditions at high latitudes. A survey of ICMEs from observations of near-Earth spacecraft and *Ulysses* shows that these spacecraft are generally separated within 40° in latitude when they observe the same CME-driven shock (Liu et al. 2005, 2006b). Reisenfeld et al. (2003) report an ICME, as well as a preceding shock, observed at both *ACE* and *Ulysses* with a latitudinal separation of 73° (comparable to the present one), but the longitudinal separation of the spacecraft is only 64°, much smaller than that in the current case. At the time of the Bastille Day event in 2000, *Ulysses* was 65° south and 116° east of the Earth, which is comparable to but smaller than the present spacecraft separation; the shock, as well as the ICME, however, did not reach *Ulysses* (Zhang et al. 2003). During the record-breaking Halloween storm in 2003, the spacecraft that observed the preceding shock were all at low latitudes (Richardson et al. 2005). Other documented events in the last 150 years either occurred before the space era or were associated with spacecraft separations that were smaller than the current one (Burlaga 1995; Cliver & Svalgaard 2004; Gopalswamy et al. 2005; Richardson et al. 2002, 2006).

Tracking the interplanetary transport of CME-driven shocks (as well as measuring their global scale) is of critical importance for solar, heliospheric, and magnetospheric studies and space weather forecasting. We draw particular attention to the CME/shock propagation, combining coronagraph images, type II bursts, in situ measurements, and the MHD model. The height-time profile is deduced from the frequency drift of the type II bands and the shock parameters measured at 1 AU, with the assumption of a kinematic model; uncertainties in the frequency drift are minimized by the constraints from 1 AU data. The shock is tracked remarkably well by the height-time curve, as cross-verified by LASCO data, the MHD model output at different distances, and *Ulysses* observations. The CME/shock has a radial speed of 2212 km s^{-1} near the Sun; the effective deceleration is about -34.7 m s^{-2} and lasts for 9.5 hr, corresponding to a transit distance of 0.36 AU. These results demonstrate that a shock can be tracked from the Sun all the way to 1 AU (and larger distances) by combining MHD propagation of the solar wind and type II emissions, a crucial technique with which to predict the shock arrival time at the Earth with small ambiguities, especially when in situ measurements closer to the Sun become available from the *Solar Orbiter* and *Solar Sentinels*.

The research was supported by the *STEREO* project under grant NAS5-03131. We acknowledge the use of *SOHO*, *GOES*, *ACE*, *WIND*, and *Ulysses* data and CME parameters from the LASCO CME catalog maintained by NASA and the Catholic University of America in cooperation with the Naval Research Laboratory (NRL). We thank C. T. Russell for helping to maintain the *STEREO* MAG data and are grateful to the referee for his or her helpful suggestions. This work was also supported in part by grant NNSFC 40621003.

REFERENCES

Acuña, M. H., Curtis, D., Scheifele, J. L., Russell, C. T., Schroeder, P., Szabo, A., & Luhmann, J. G. 2008, Space Sci. Rev., 136, 203
Biesecker, D. A., Myers, D. C., Thompson, B. J., Hammer, D. M., & Vourlidas, A. 2002, ApJ, 569, 1009
Burlaga, L. F. 1995, Interplanetary Magnetohydrodynamics (New York: Oxford Univ. Press)
Cane, H. V., Sheeley, N. R., Jr., & Howard, R. A. 1987, J. Geophys. Res., 92, 9869
Cliver, E. W., & Svalgaard, L. 2004, Sol. Phys., 224, 407
Dungey, J. W. 1961, Phys. Rev. Lett., 6, 47
Gopalswamy, N., Lara, A., Yashiro, S., Kaiser, M. L., & Howard, R. A. 2001, J. Geophys. Res., 106, 29207
Gopalswamy, N., Yashiro, S., Krucker, S., Stenborg, G., & Howard, R. A. 2004, J. Geophys. Res., 109, A12105
Gopalswamy, N., Yashiro, S., Liu, Y., Michalek, G., Vourlidas, A., Kaiser, M. L., & Howard, R. A. 2005, J. Geophys. Res., 110, A09S15
Hau, L.-N., & Sonnerup, B. U. Ö. 1999, J. Geophys. Res., 104, 6899
Hu, Q., & Sonnerup, B. U. Ö. 2002, J. Geophys. Res., 107, 1142

Kahler, S. W., & Reames, D. V. 1991, J. Geophys. Res., 96, 9419
Kosovichev, A. G., & Sekii, T. 2007, ApJ, 670, L147
Lario, D., Decker, R. B., Livi, S., Krimigis, S. M., Roelof, E. C., Russell, C. T., & Fry, C. D. 2005, J. Geophys. Res., 110, A09S11
Larson, D. E., et al. 1997, Geophys. Res. Lett., 24, 1911
Li, Y., Lynch, B. J., Welsch, B. T., Stenborg, G. A., Vourlidas, A., Luhmann, J. G., & Fisher, G. H. 2007, AGU Fall Meeting, abstr. SH32A-0773
Lin, R. P., Evans, L. G., & Fainberg, J. 1973, Astrophys. Lett., 14, 191
Lin, R. P., et al. 2008, Space Sci. Rev., 136, 241
Liu, Y., Luhmann, J. G., Huttunen, K. E. J., Lin, R. P., Bale, S. D., Russell, C. T., & Galvin, A. B. 2008, ApJ, 677, L133
Liu, Y., Richardson, J. D., & Belcher, J. W. 2005, Planet. Space Sci., 53, 3
Liu, Y., Richardson, J. D., Belcher, J. W., & Kasper, J. C. 2007, ApJ, 659, L65
Liu, Y., Richardson, J. D., Belcher, J. W., Kasper, J. C., & Skoug, R. M. 2006a, J. Geophys. Res., 111, A09108, DOI:10.1029/2006JA011723
Liu, Y., Richardson, J. D., Belcher, J. W., Wang, C., Hu, Q., & Kasper, J. C. 2006b, J. Geophys. Res., 111, A12S03, DOI:10.1029/2006JA011890
Luhmann, J. G., et al. 2008, Space Sci. Rev., 136, 117
Malandraki, O. E., Lario, D., Lanzerotti, L. J., Sarris, E. T., Geranios, A., & Tsiropoula, G. 2005, J. Geophys. Res., 110, A09S06
McKibben, R. B., et al. 2005, J. Geophys. Res., 110, A09S19
Mewaldt, R. A., et al. 2008, Proc. 30th Int. Cosmic Ray Conf. (Merida), in press
Müller-Mellin, R., et al. 2008, Space Sci. Rev., 136
Mulligan, T., Blake, J. B., & Mewaldt, R. A. 2008, Proc. 30th Int. Cosmic Ray Conf. (Merida), in press
Nelson, G. J., & Melrose, D. B. 1985, in Solar Radiophysics: Studies of Emission from the Sun at Metre Wavelengths, ed. D. J. McLean & N. R. Labrum (Cambridge: Cambridge Univ. Press), 333
Neupert, W. M. 1989, ApJ, 344, 504
Reiner, M. J., Kaiser, M. L., & Bougeret, J.-L. 2001, J. Geophys. Res., 106, 29989
———. 2007, ApJ, 663, 1369
Reisenfeld, D. B., Gosling, J. T., Forsyth, R. J., Riley, P., & St. Cyr, O. C. 2003, Geophys. Res. Lett., 30, 8031
Richardson, J. D., Paularena, K. I., Wang, C., & Burlaga, L. F. 2002, J. Geophys. Res., 107, 1041
Richardson, J. D., Wang, C., Kasper, J. C., & Liu, Y. 2005, Geophys. Res. Lett., 32, L03S03
Richardson, J. D., et al. 2006, Geophys. Res. Lett., 33, L23107
Sauvaud, J.-A., et al. 2008, Space Sci. Rev., 136, 227
Schindler, K., Pfirsch, D., & Wobig, H. 1973, Plasma Phys., 15, 1165
Sturrock, P. A. 1994, Plasma Physics: An Introduction to the Theory of Astronomical, Geophysical and Laboratory Plasmas (Cambridge: Cambridge Univ. Press)
Thompson, B. J., Plunkett, S. P., Gurman, J. B., Newmark, J. S., St. Cyr, O. C., & Michels, D. J. 1998, Geophys. Res. Lett., 25, 2465
Viñas, A. F., & Scudder, J. D. 1986, J. Geophys. Res., 91, 39
Vourlidas, A., Wu, S. T., Wang, A. H., Subramanian, P., & Howard, R. A. 2003, ApJ, 598, 1392
Wang, C., Richardson, J. D., & Gosling, J. T. 2000, J. Geophys. Res., 105, 2337
Wang, C., Richardson, J. D., & Paularena, K. I. 2001, J. Geophys. Res., 106, 13007
Wang, Y., Zhou, G., Ye, P., Wang, S., & Wang, J. 2006, ApJ, 651, 1245
Zarro, D. M., Sterling, A. C., Thompson, B. J., Hudson, H. S., & Nitta, N. 1999, ApJ, 520, L139
Zhang, J., Li, L., & Song, Q. 2007, ApJ, 662, L35
Zhang, M., McKibben, R. B., Lopate, C., Jokipii, J. R., Giacalone, J., Kallenrode, M.-B., & Rassoul, H. K. 2003, J. Geophys. Res., 108, 1154